Application of the finite element method to aeroelasticity

Jean-Pierre Grisval — Cédric Liauzun

Office National d'Etudes et de Recherches Aérospatiales
B.P. 72, F-92322 Châtillon cedex
Email : {grisval, liauzun}@onera.fr
Web : www.onera.fr

ABSTRACT. *This paper presents a multiphysic method for unsteady turbulent flows and fluid-structure computations. This method is based on a Galerkin Least Square Finite Element formulation for both solid and fluid equations. The viscous effects are taken into account using Spalart-Allmaras and k-ε turbulence models. The fluid boundaries motion is taken into account using an ALE formulation of the compressible equations. The fluid domain is then modeled as a hyperelastic material. For fluid-structure interactions problems, both solid and fluid equations are time discretized using an implicit time-stepping scheme based on the Newmark's one. Coupling between fluid and structure is achieved through non-matching interfaces. This numerical strategy is applied to a 2D airfoil buffeting simulation, to a 2D fluid-structure computation, and to a flutter analysis of a 3D wing.*

RÉSUMÉ. *Cet article présente une méthode multiphysique de calcul d'écoulements instationnaires turbulents, et d'étude de couplage fluide-structure. Cette méthode s'appuie sur une formulation Eléments Finis Galerkin Moindres Carrés des équations de la mécanique des solides, d'Euler ou de Navier Stokes. Les effets de la viscosité sont pris en compte par l'utilistation des modèles de turbulence Spalart-Allmaras et k-ε. Le mouvement des frontières du domaine fluide est pris en compte par l'écriture des équations du problème fluide dans un référentiel ALE. Le domaine fluide est alors considéré comme un matériau hyperélastique. Pour l'étude des interactions fluide-structure, les équations du solide et du fluide sont discrétisées en temps par un schéma implicite dérivé de celui de Newmark. Un algorithme d'interfaçage transmet les contraintes d'un problème à l'autre à chaque pas de temps. Cette stratégie numérique est appliquée à l'étude du buffeting d'un profil 2D, du couplage fluide-structure pour un profil 2D, et du flottement d'une aile d'avion tridimensionnelle.*

KEY WORDS : *Finite Element Method, turbulence models, ALE formulation, aeroelasticity.*

MOTS-CLÉS : *Méthode des éléments finis, modèles de turbulence, formulation ALE, aeroéasticité.*

Revue européenne des éléments finis. Volume 8 – n° 5-6/1999, pages 553 à 579

1. Introduction

Aeroelasticity studies involving fluid-structure interactions problems and predictions of unsteady airloads on wings play an increasing role in the aircraft design. With the increasing power of computers, several numerical methods have been developed to predict time responses of a wing or an airfoil to different excitations. This paper presents a numerical method for performing fluid-structure time simulations with turbulent viscous flow models. This method is evaluated for unsteady viscous phenomena like buffeting, and for fluid-structure interactions. It is based on the Galerkin Least Square Finite Element formulation of both aerodynamic and structural equations. It is therefore able to handle unstructured meshes that are more useful to model complex geometries. In order to take into account the viscous effects, two turbulence models have been used:

— the Spalart-Allmaras model, which is a one-equation model solving for the turbulent kinematic viscosity

— the classical two-equation k-ε model.

Wall functions have been added to both turbulence models in order to reduce mesh size and CPU time, and to perform three-dimensional simulations with a reasonable number of mesh nodes.

For fluid-structure interactions problems, the compressible Navier-Stokes equations are written in an ALE frame of reference to take into account the deformation of the structure embedded in the fluid domain.

All simulations have been performed using the software Spectrum developed and commercialized by Centric Engineering Systems, Inc. It uses the numerical strategy presented above to solve the solid mechanics and the compressible Euler or Navier-stokes equations.

An outline of this paper follows: the second part presents a description of the numerical techniques relevant to fluid-structure interactions problems. The third part presents numerical results compared with experimental data. A buffeting simulation with 2D airfoils, and fluid-structure simulations with 2D airfoils and a 3D wing to predict flutter are treated.

2. Numerical approach

The numerical strategy developed to perform fluid-structure simulations involves the solution of several problems (also referred to as "staggers"):

— unsteady flow around structure

— turbulent eddy viscosity

— deformation of the fluid mesh

— dynamic analysis of the structural model

— coupling between fluid and structural problems

Each of these problems is detailed in the sections below, followed by a description of the solution strategy applied to fluid-structure simulation.

2.1. *Fluid analysis*

The compressible Navier-Stokes equations written in a arbitrary Lagriagian-Eulerian frame of reference are used to model the fluid flow:

$$\boldsymbol{U}_{,t} + w_{i,i}\boldsymbol{U} + \boldsymbol{F}_{i,i} - \boldsymbol{F}_{i,i}^{\text{diff}} = \boldsymbol{0} \qquad [1]$$

where

$$\boldsymbol{U} = \rho \begin{Bmatrix} 1 \\ \boldsymbol{u} \\ e + \|\boldsymbol{u}\|^2/2 \end{Bmatrix} \qquad [2]$$

$$\boldsymbol{F}_i = (u_i - w_i)\boldsymbol{U} + p \begin{Bmatrix} 0 \\ \boldsymbol{\delta}_i \\ u_i \end{Bmatrix} \qquad [3]$$

$$\boldsymbol{F}_i^{\text{diff}} = \begin{Bmatrix} 0 \\ \tau_{ij}\boldsymbol{\delta}_j \\ \tau_{ij}u_j - q_i \end{Bmatrix} \qquad [4]$$

$\boldsymbol{U}$ is the vector of conservative variables; $\boldsymbol{F}_i$ and $\boldsymbol{F}_i^{\text{diff}}$ are the convective and diffusive fluxes in direction i, respectively; ρ is the fluid density; $\boldsymbol{u} = \{u_i\}$ is the fluid velocity; e^{tot} is the total energy per unit mass; p is the pressure; $\boldsymbol{\delta}_i = \{\delta_{ij}\}$ is the Kronecker delta ($\delta_{ii} = 1$ and $\delta_{ij} = 0$ for $i \neq j$); $\boldsymbol{\tau} = [\tau_{ij}]$ is the viscous stress tensor; $\boldsymbol{q} = \{q_i\}$ is the heat flux vector; and $\boldsymbol{w} = \{w_i\}$ is the mesh velocity. Moreover, the fluid is modeled as an ideal gas and the stress tensor is that of a Newtonian fluid.

$$\tau_{ij} = \lambda u_{k,k}\delta_{ij} + \mu(u_{i,j} + u_{j,i}) \qquad [5]$$

where λ is determined by the Stokes law ($\lambda + 2\mu/3 = 0$) and μ by the Sutherland's law. The heat flux is given by the Fourier's law:

$$q_i = -\kappa T_{,i} \qquad [6]$$

Equation [1] reduces to the compressible Euler equations by setting $\boldsymbol{F}_i^{\text{diff}} = \boldsymbol{0}$. Both pure Eulerian and pure Lagrangian formulations can be recovered by setting $\boldsymbol{w} = \boldsymbol{0}$ or $\boldsymbol{w} = \boldsymbol{u}$, respectively. A change of variables is applied to [1] by using the so-called "entropy variables", leading to a symmetric form of the Navier-Stokes equations [HFM 86].

$$\boldsymbol{V} = \frac{1}{T} \begin{Bmatrix} \tilde{\mu} - \|\boldsymbol{u}\|^2/2 \\ \boldsymbol{u} \\ -1 \end{Bmatrix} \qquad [7]$$

where $\tilde{\mu}$, the chemical potential, is defined as

$$\tilde{\mu} = e + p/\rho - Ts$$

and s is the specific entropy. Written in terms of theses variables, the compressible Navier-Stokes equation [1] yields the symmetric convective-diffusive form

$$\widetilde{\boldsymbol{A}}_0 \boldsymbol{V}_{,t} + \widetilde{\boldsymbol{A}}_i \boldsymbol{V}_{,i} - (\widetilde{\boldsymbol{K}}_{ij} \boldsymbol{V}_{,j})_{,i} = \boldsymbol{0} \qquad [8]$$

where:

— $\widetilde{\boldsymbol{A}}_0$ is symmetric positive-definite

— $\widetilde{\boldsymbol{A}}_i$ is symmetric for $i = 1, 3$

— $\widetilde{\boldsymbol{K}} = [\widetilde{\boldsymbol{K}}_{ij}]$ is symmetric positive-semidefinite.

There are three major advantages to this system due to symmetry properties:

— they contribute to the efficiency of iterative solution strategies,

— they are essential for the development of the stability terms of the GLS formulation,

— they are useful for mathematical analysis for stability and convergence.

Spatial discretization of the Navier-Stokes equations is done using the Galerkin/least-squares (GLS) finite element formulation [HFH 89]. Consider a physical domain Ω with boundary $\Gamma = \partial\Omega$ discretized with elements Ω^e. The GLS formulation is

$$\begin{aligned} &\int_\Omega (\boldsymbol{W} \cdot \boldsymbol{U}_{,t} - \boldsymbol{W}_{,i} \cdot \boldsymbol{F}_i + \boldsymbol{W}_{,i} \cdot \boldsymbol{F}_i^{\text{diff}})\, d\Omega \\ &+ \textstyle\sum_e \int_{\Omega^e} \mathcal{L}\boldsymbol{W} \cdot \boldsymbol{\tau} \mathcal{L}\boldsymbol{V}\, d\Omega \\ &+ \textstyle\sum_e \int_{\Omega^e} \nu^e g^{ij} \boldsymbol{W}_{,i} \cdot \widetilde{\boldsymbol{A}}_0 \boldsymbol{V}_{,j}\, d\Omega \\ &= \int_\Gamma \boldsymbol{W} \cdot (\boldsymbol{F}_i - \boldsymbol{F}_i^{\text{diff}}) n_i\, d\Omega \end{aligned} \qquad [9]$$

where $\boldsymbol{W}$ is the weighting function, $\boldsymbol{n} = \{n_i\}$ is the outward normal, $\boldsymbol{\tau}$ is a symmetric positive-definite matrix (for more details, see [HFM 87]), $g^{ij} = [\partial x_i / \partial \xi_j]$ is the jacobian matrix of the element Ω^e, and $\mathcal{L}$ is the Navier-Stokes linear functional defined as:

$$\mathcal{L} = \widetilde{\boldsymbol{A}}_0 \frac{\partial}{\partial t} + \widetilde{\boldsymbol{A}}_i \frac{\partial}{\partial x_i} - \frac{\partial}{\partial x_i} \left(\widetilde{\boldsymbol{K}}_{ij} \frac{\partial}{\partial x_j} \right) \qquad [10]$$

and ν^e is a positive coefficient depending on $\mathcal{L}\boldsymbol{V}$. The first and the last terms of the variational equation [9] are the terms of the classical Galerkin formulation written in an integrated-by-parts form to guarantee flux conservation in the flowfield. The second integral term is the Least Square term that allows us to obtain an oscillation-free solutions in advection-dominated regions [HFM 87]. The third integral term is a shock-capturing term to eliminate spurious oscillations near shocks and sharp gradients [HM 86]. Stability and consistency of the resulting formulation imply a higher-order spatial convergence.

Time discretization is done using the Hilbert-Hughes-Taylor (HHT) algorithm [HU 87] based on Newmark's implicit scheme. This parameter-based semi-discrete

technique encompasses a wide range of implicit first- and second-order time-marching schemes such as backward Euler and trapezoidal rule.

Both spatial and temporal discretizations of the finite element formulation lead to a nonlinear system of equations to be solved at each time-step. This system is linearized through a Newton-like algorithm, yielding a series of nonsymmetric linear systems of equations. Each system is solved using a matrix-free implicit iterative solver based on the preconditioned GMRES algorithm with a tolerance ranging from 10^{-1} for static problems to 10^{-2} for dynamic problems [JOH 91].

2.2. *Turbulence models*

In order to take into account the viscous effects, turbulence models are added to the density-weighted Navier-Stokes equations, id est

$$
\begin{aligned}
&\overline{\rho}_{,t} + (\overline{\rho}\widetilde{u}_i)_{,i} = 0 \\
&(\overline{\rho}\widetilde{u}_i)_{,t} + \left[\overline{\rho}\widetilde{u}_i\widetilde{u}_j + (\overline{p} + \tfrac{2}{3}\overline{\rho}k)\delta_{ij}\right]_{,j} = \left[(\mu + \mu_t)\Big((\widetilde{u}_i)_{,j} + (\widetilde{u}_j)_{,i} + \frac{\lambda}{\mu}\delta_{ij}(\widetilde{u}_l)_{,l}\Big)\right]_{,j} \\
&(\overline{\rho}\widetilde{e}_{tot})_{,t} + \left[\overline{\rho}\widetilde{u}_i\widetilde{e}_{tot} + (\overline{p} + \tfrac{2}{3}\overline{\rho}k)\widetilde{u}_i\right]_{,i} = \\
&\qquad \left[(\mu + \mu_t)\Big((\widetilde{u}_i)_{,j} + (\widetilde{u}_j)_{,i} + \frac{\lambda}{\mu}\delta_{ij}(\widetilde{u}_l)_{,l}\Big)\widetilde{u}_j + (\kappa + \kappa_t)\widetilde{T}_{,i} + \Big(\mu + \frac{\mu_t}{Pr_k}\Big)k_{,i}\right]_{,i}
\end{aligned}
\qquad [11]
$$

where for any quantity φ, $\overline{\varphi}$ is the time mean value of φ, $\widetilde{\varphi} = \frac{\overline{\rho\varphi}}{\overline{\rho}}$, $\kappa_t = c_p\frac{\mu_t}{Pr_t}$, Pr_k is a modeling constant, and Pr_t is assumed constant. To close the system, turbulence models solve equations for the turbulent eddy viscosity μ_t, and the turbulent kinetic energy k.

Two turbulence models have been used in this study: the classical two-equation k-ε model and the Spalart-Allmaras model.

The k-ε model is a "low Reynolds" model based on the Chien's formulation [CHI 82, LAU 74]. It solves a system of coupled partial differential equations within k-ε. μ_t is then computed from a relation $\mu_t = f(y^+)\overline{\rho}\frac{k^2}{\varepsilon}$. The variables k and ε are computed in down to the wall, thus requiring a very fine mesh near the no-slip wall. The first grid point away from wall should be such that $y^+ < 0.5$. The partial differential equations within k-ε are coupled. They are solved using a GLS formulation like the one for the Navier-Stokes equations. But the turbulence equations are uncoupled from the Navier-Stokes equations and solved in a staggered fashion. The linearized systems from the turbulence equations are solved using a GMRES algorithm.

The Spalart-Allmaras model [SPA 92] was developed by Boeing at the beginning of the 1990's to compute external turbulent flows. It is a one-equation model that

governs the kinematic viscosity, and assumes $k = 0$ in equations [11]. We can note that:

— The model does not require the knowledge of any non local quantity like thickness of the boundary layer. It is then more useful for unstructured meshes than algebraic models like the Baldwin-Lomax model.

— The kinematic viscosity is linear close to the no-slip wall. The model therefore requires less refined meshes than the k-ε model to reach the same accuracy. Reasonable solutions can be obtained with the first grid point as far away from the wall as $y^+ = 5$ to 10 and $y^+ = 20$ if only pressure is of interest.

— The model is based on only one equation to solve. It is considerably less expensive computationally than the k-ε model. Moreover the use of iterative solvers is easier.

In order to perform three-dimensional simulations with a reasonable number of mesh nodes, wall functions have been implemented for both turbulence models. In the wall function approximation, the fluid is assumed to follow the "law of the wall" in the finite elements adjacent to solid boundaries. In these elements, the flow is determined by Spalding's law [WHI 91]:

$$y^+ = u^+ + e^{-\kappa B}\left(e^{\kappa u^+} - 1 - \kappa u^+ - \frac{(\kappa u^+)^2}{2} - \frac{(\kappa u^+)^3}{6}\right) \qquad [12]$$

with $y^+ = \rho y u^* / \mu$; $u^+ = \|\boldsymbol{u}\| / u^*$; $\kappa = 0.41$ et $B = 5.0$. The values of y and $\|\boldsymbol{u}\|$ being known, the shear velocity is deduced from (12) with a Newton method. The wall friction is given by

$$\boldsymbol{\tau}_n = -\rho {u^*}^2 \frac{\boldsymbol{u}}{\|\boldsymbol{u}\|} \qquad [13]$$

This approximation leads to having both a slip-velocity Dirichlet boundary condition to satisfy the condition of zero mass flux, and a friction Neuman boundary condition by specifying

$$\int_{\Gamma_{wall}} \boldsymbol{F}_i^{diff} n_i d\Gamma = \int_{\Gamma_{wall}} \left\{ \begin{array}{c} 0 \\ \boldsymbol{\tau}_n \\ \boldsymbol{\tau}_n \cdot \boldsymbol{u} - q_n \end{array} \right\} d\Gamma \qquad [14]$$

where q_n is the heat flux at wall.

2.3. *Mesh movement*

The use of an ALE formulation calls for a strategy to deform the fluid mesh as the fluid domain boundaries move. Such motions can be either prescribed or they can result from deformations of solids immersed in the fluid domain. The mesh deformation approach used in this study models the fluid domain as a hyperelastic material (i.e., a rubber-like material) and uses a large-deformation neo-hookean formulation ([SPE 93]). Displacements of mesh nodes are computed using a preconditioned

conjugate gradient algorithm with a tolerance usually of the order of 10^{-3}. Once the displacements are obtained, the mesh velocity at each node is computed using the formula

$$\boldsymbol{w}_{n+1} = -\boldsymbol{w}_n + \frac{2}{\Delta t}(\boldsymbol{d}_{n+1} - \boldsymbol{d}_n) \qquad [15]$$

where $\boldsymbol{d}_n$ ($\boldsymbol{w}_n$) and $\boldsymbol{d}_{n+1}$ ($\boldsymbol{w}_{n+1}$) are node displacements (velocities) at time t_n and t_{n+1}, respectively; and $\Delta t = t_{n+1} - t_n$. Equation [15] leads to mass conservation in the fluid domain, as shown by Farhat *et al.* [FAR 95]. One should note that no mesh deformation technique (including the one used herein) guarantees mesh integrity for general boundary motions. Negative element jacobians can indeed occur when very large deformations or twisting motions are simulated. The hyperelastic model has however proven to be more robust in that respect than simpler strategies such as modeling the fluid domain with a network of springs (see [BAT 89] for an example of such techniques) or using a simple linear elasticity formulation.

2.4. *Structural analysis*

A large-deformation elasticity formulation is used to model the structural part of aeroelastic problems [SPE 93]. Structures can be modeled either with three-dimensional continuum elements, or with structural elements such as shells, beams or trusses. Time-marching is performed with an implicit integrator based on the HHT algorithm. This semi-discrete scheme is identical to the one used for the fluid equations, which simplifies the overall time-marching process when solving coupled aeroelastic problems. Due to ill-conditioning that arises when the solid is discretized with non-continuum elements, a sparse direct solver is used to solve the linear systems of equations resulting from discretization of the variational formulation.

2.5. *Fluid-solid interface*

The interface region between the fluid domain and the solid domain is defined by:

— a list of nodes and element faces on the fluid side; and

— a list of nodes and element faces on the solid side.

Since nodes on both sides of the interface do not need to match, a search algorithm is used to identify the solid face that contains each fluid interface node. Once this mapping is obtained, local fluid pressure forces are computed at each fluid interface node. They are then interpolated at the solid interface nodes. The resulting pressure load is used as a boundary condition to solve the structural analysis problem. One can note that this approach leads to a total fluid pressure force (i.e., the pressure integrated over the fluid side of the interface) being transferred to the solid side of the interface. Since the fluid mesh is usually finer than the solid mesh (which translates into having a finer fluid surface mesh at the fluid-solid interface), this interpolation strategy would

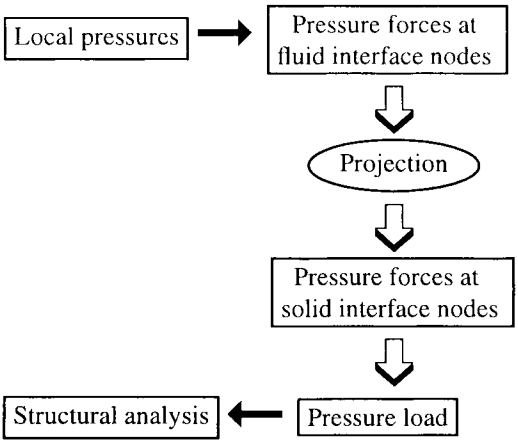

Figure 1. *Fluid-solid interfacing flowchart*

appear to be more accurate than interpolating the fluid pressure directly onto the solid interface nodes and then computing the local pressure forces on that surface using the solid discretization.

In addition to pressure loading on the solid, a velocity boundary condition is applied at the fluid interface nodes. This boundary condition is:

— $\boldsymbol{u} = \boldsymbol{w}$ for a no-slip boundary condition; or

— $(\boldsymbol{u} - \boldsymbol{w}) \cdot \boldsymbol{n} = 0$ for a slip boundary condition.

Finally, the solid displacement is interpolated at the fluid interface nodes and is used as a boundary condition when solving the mesh deformation problem.

2.6. *Solution strategy*

Studies carried out on two-dimensional problems have shown that the order in wich the different staggers are solved at each time step has an impact on the overall solution accuracy. Several remarks can be made about the results we obtained:

— The flow field should be computed before turbulent fields at each time step.

— For fluid-structure problems, the fluid mesh needs to be defined for the computational domain $\Omega(t_{n+1})$ when advancing the fluid solution from t_n to t_{n+1}. Consequently, the mesh deformation problem should be solved before the fluid problem at each time step.

— Since the solid motion is driving the fluid mesh deformation, the structural analysis problem should be solved before the mesh deformation problem.

Consequently, the most accurate procedure for fluid-structure problems is as follows:

Loop over time steps

— 1. Solve the structural analysis problem using the fluid pressure at the previous time step as a boundary condition.

— 2. Solve the fluid mesh deformation problem using the structural displacement as a boundary condition.

— 3. Solve the fluid problem using the mesh velocity as a boundary condition.

End loop over time steps

Only one iteration is performed on the three staggers within each time step for computational efficiency.

3. Numerical examples

3.1. *Buffeting simulation*

The numerical strategy described in the previous part is applied to buffeting simulations with a RA16SC1 airfoil in transonic flow. Experiments in a wind tunnel at ONERA show oscillations of the shock at a single frequency of about 100 Hz for a Mach of 0.73 and an angle of attack greater than 3 degrees. The amplitude of the oscillations is about 40% of chord.

Numerical simulations have been led for the following free-stream conditions:

— $M_\infty = 0.73$

— $Re_\infty = 4.6 \times 10^6$

— $T_{i\infty} = 290.0$ K.

The airfoil chord is 180 mm.

Two numerical simulations at an angle of attack of 3 degrees are done to test the Spalart-Allmaras and k-ε models without wall functions. The first simulation uses the Spalart-Allmaras model. The fluid domain is discretized with 17538 nodes and 17180 wedge elements. Even though this is a two-dimensional problem, three-dimensional meshes made of one layer of elements together with appropriate boundary conditions are generated since the used software Spectrum has only three-dimensional capabilities. The following boundary conditions are applied:

— velocity and static temperature at the inflow

— static pressure at the outflow

— no slip velocity at the wall.

A steady flow is first computed using a local time-stepping and a CFL set to 5. The solution converges at the 200^{th} time-step. A unsteady computation is restarted from the steady solution using a global time-step. The experimental frequency f_0 being

about 108 Hz, the numerical time increment is chosen such that

$$\Delta t = \frac{1/f_0}{1000} = 9.2 \times 10^{-6} \text{ s}$$

The computation does not show any buffeting. The shock oscillations in global time-stepping are rapidly damped. Similar results are obtained on finer meshes or at a greater angle of attack. The Spalart-Allmaras model developed for steady computations does not seem to be appropriate for buffeting simulations.

The second computation using the k-ε model follows the same strategy. The mesh is refined close to wall and contains 25396 nodes and 25014 elements (see figure 2). The local time-step is determined by a CFL equal to 3. The steady computation does not converge (oscillations of residuals of pressure velocity and temperature). The computation is restarted with a global time increment chosen to have 4000 time-steps per period id est $\Delta t = 2.3 \times 10^{-6}$ s. The results illustrated by figures 4 and 5 show that the shock oscillates between 35% and 60% of chord with a frequency of 95 Hz, that is of the order of the experimental data. The numerical frequency is computed with a poor resolution, that depend on the duration of the computation. Because of the great number of time-steps per period, a small number of periods could have been computed. Moreover, no correction on the mach or the angle of attack have been considered to take into account the wall effects in the wind tunnel. Those effects could have an influence on the shock oscillations.

3.2. *Buffeting of the DYVAS Airfoil*

The same computation is done with a 2D airfoil that is deduced from the 3D wing using similarity relations and corresponds to the section at 66% of wing. The similarity relations give the flow conditions:

$$\left\{ \begin{array}{rcl} M_{3D\infty} & = & 0.82 \\ Re_{3D} & = & 2 \times 10^6 \\ \alpha_{local3D} & = & 2.72^\circ \end{array} \right. \longrightarrow \left\{ \begin{array}{rcl} M_{2D\infty} & = & 0.737 \\ Re_{3D} & = & 1.165 \times 10^6 \\ \alpha_{local2D} & = & 3.02^\circ \end{array} \right.$$

The k-ε model with wall functions is used with a mesh of 14884 nodes and 14546 elements. The first layer is 5×10^{-4}chord thick (figure 6).

The first 1500 time-steps are computed with local time-stepping and CFL set to 3. The following time-steps are computed with a global time increment such that

$$\Delta t = \frac{1/f_0}{2000} = 1.0 \times 10^{-5} \text{ s}$$

where the experimental shock oscillation frequency is $f_0 = 50Hz$.
The computed frequency of the oscillations of lift is 45 Hz, close to the experimental results (see figures 7 and 8).

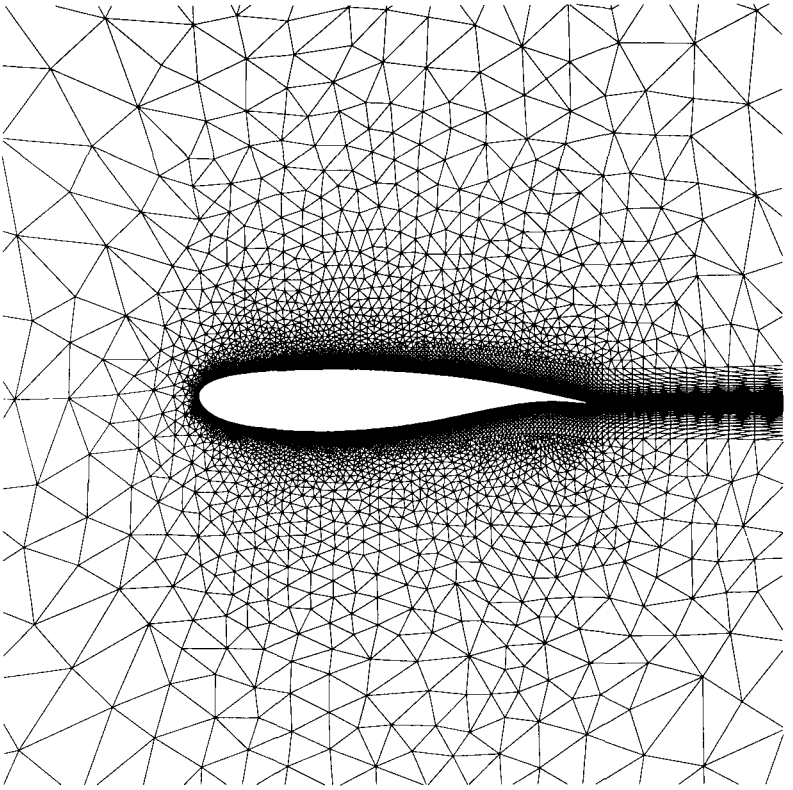

Figure 2. *Fluid mesh around RA16SC1 airfoil*

For the next simulation with the same model, a pitching motion is imposed on the airfoil following the law:

$$\begin{cases} \alpha(t) = \alpha_{2D\infty} + \alpha_{ampl} \sin^2(2\pi f t) & \text{for } t < 1/(4f) \\ \alpha(t) = \alpha_{2D\infty} + \alpha_{ampl} \sin(2\pi f t) & \text{for } t \geq 1/(4f) \end{cases}$$

where $\alpha_{ampl} = 0.2°$. The law in $\sin^2$ allows a zero initial velocity. The unsteady simulation is initialized with a steady case for an angle of attack of $\alpha_{2D\infty}$. This case is computed for the frequencies $f = 40$ Hz and $f = 60$ Hz with a global time increment $\Delta t = 10^{-5}$ s. The computed lift frequencies for the cases at 40 Hz and 60 Hz are respectively 42 Hz and 47 Hz (figure 9).

3.3. *2D fluid-structure simulation with NACA 64A010airfoil*

The objective of this numerical example is to perform the flutter analysis of a rigid NACA 64A010 airfoil (NASA Ames model described in [DAV 83]). The fluid flow

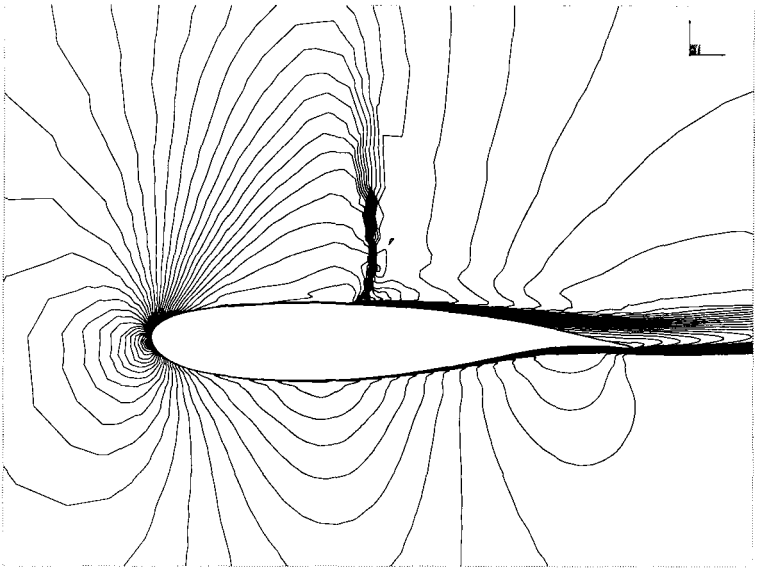

Figure 3. *Turbulent (k-ε) mach contours*

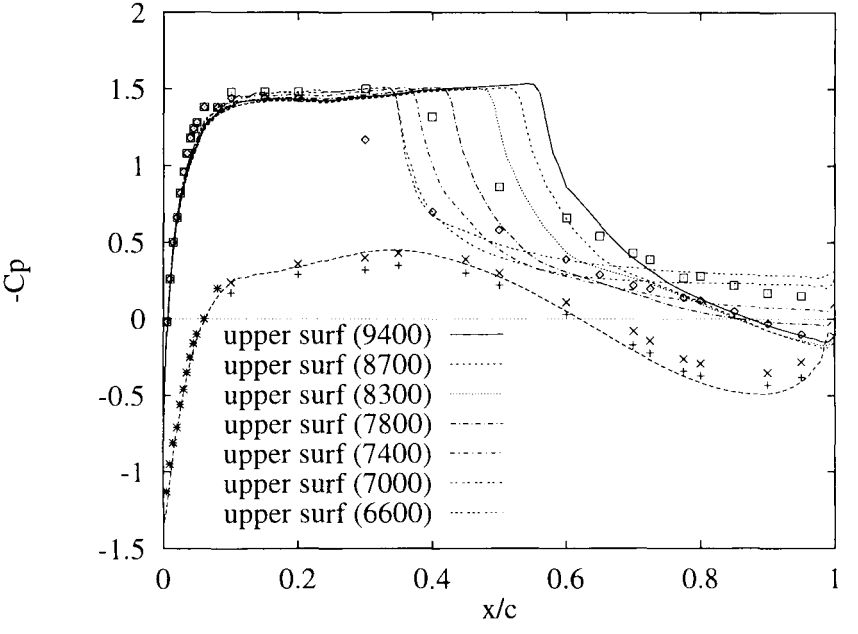

Figure 4. *Chord-wise Cp distribution*

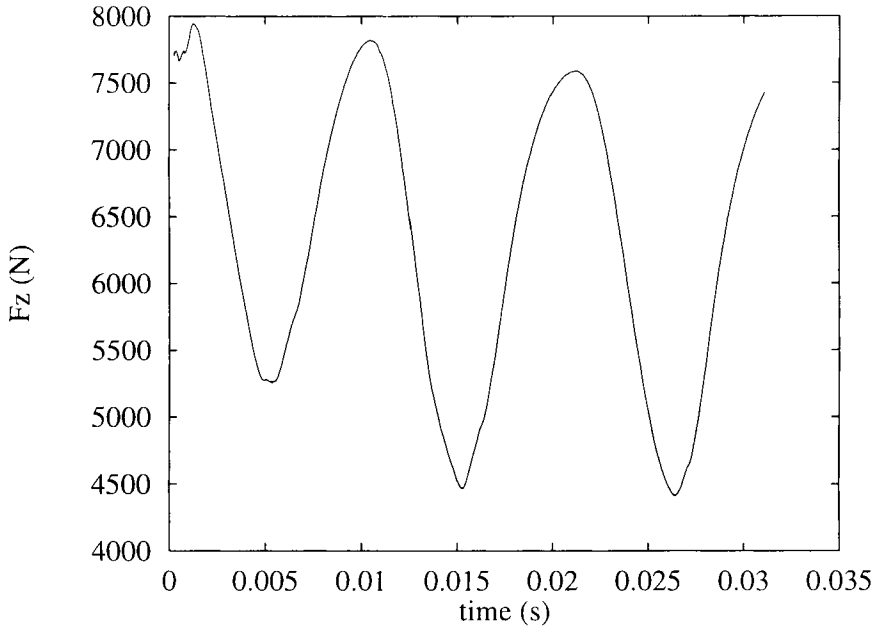

Figure 5. *Lift (k-ε model)*

has the following free-stream conditions:

— $M_\infty = 0.796$

— $u_\infty = 267.5$ m/s

— $T_\infty = 281.0$ K

— $p_\infty = 1.339 \times 10^5$ Pa

The fluid domain is discretized with 7,626 nodes and 7,344 wedges (see Figure 10 for a global view of the mesh). A steady flow is first computed solving the compressible Euler equations and using a first-order time-marching scheme with local time-stepping and a CFL number set to 5. Steady pressure contours near the airfoil are presented in Figure 11. Pressure distribution on the upper and lower surfaces of the airfoil together with a comparison with the experimental data presented in [DAV 83] is shown in Figure 12.

The solid domain is meshed with 604 nodes and 246 hexahedra (see Figure 13). The airfoil is modeled as a hypoelastic material with a very large Young's modulus ($E = O(10^{20})$ Pa) to achieve nearly perfect rigidity. The airfoil is free to rotate around a specified elastic axis. However, this axis is constrained to move only in a vertical direction. A large deformation formulation is used to simulate the airfoil displacement and rotation. Proper boundary conditions are applied to the airfoil in order to perform

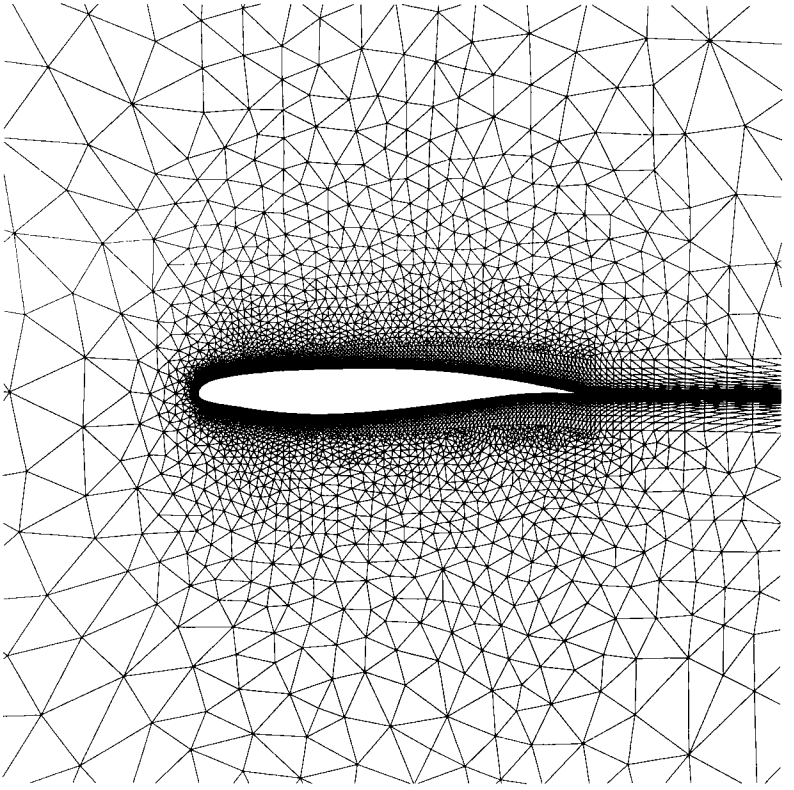

Figure 6. *Fluid mesh around Dyvas airfoil*

a simulation equivalent to a two degree-of-freedom structural problem [BIS 62] of the form

$$m\ddot{z} - S\ddot{\alpha} + k_z z = L \quad [16]$$
$$-S\ddot{z} + I\ddot{\alpha} + k_\alpha \alpha = M_y \quad [17]$$

where z is the vertical displacement; α is the rotation around the elastic axis; m is the total mass; $S = m(x_{\text{cg}} - x_{\text{axis}})$ is the static unbalance about the elastic axis; I is the mass moment of inertia about the elastic axis; k_z is the translational stiffness; k_α is the rotational stiffness; L is the aerodynamic lift; and M_y is the pitching moment ($M_y > 0$ nose-up). k_z and k_α are chosen to obtain natural translational and rotational frequencies $f_z = 1/T_z = 60$ Hz and $f_\alpha = 1/T_\alpha = 65$ Hz.

Two test cases are considered to analyze the behavior the fluid-solid system under both stable and unstable conditions. Equivalent structural characteristics of both cases are presented in Table 1. The airfoil chord is 0.5 m and the elastic axis is located at 24.8% of chord.

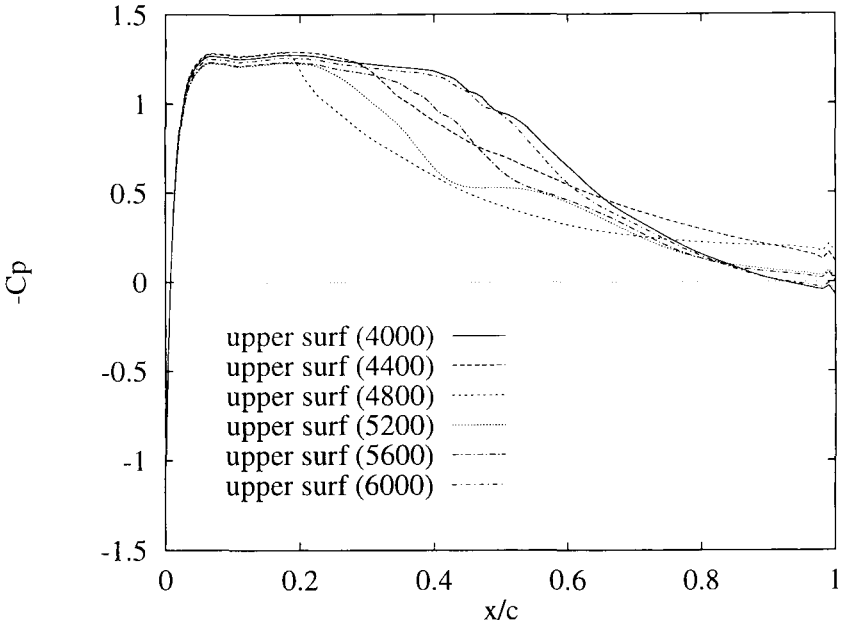

Figure 7. *Chord-wise Cp distribution*

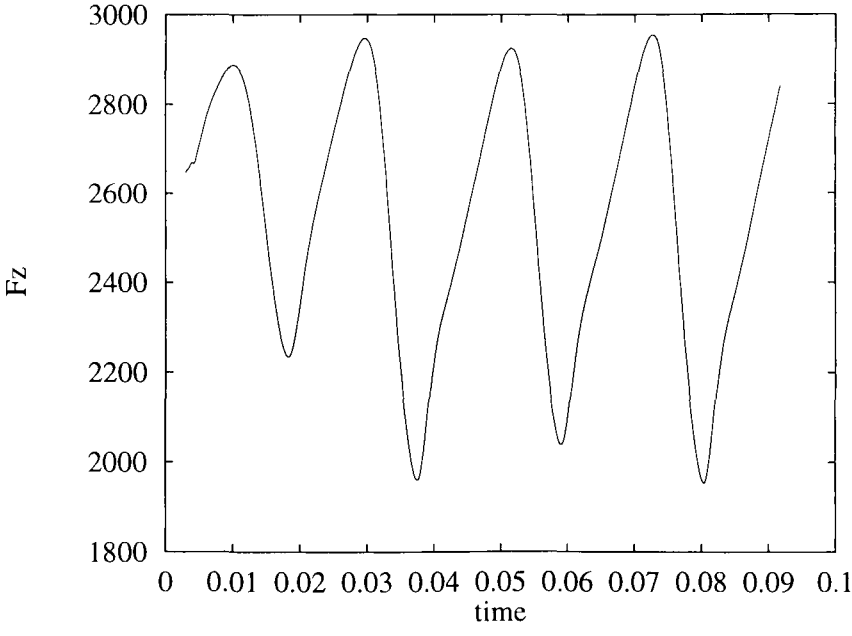

Figure 8. *Lift (k-ε model)*

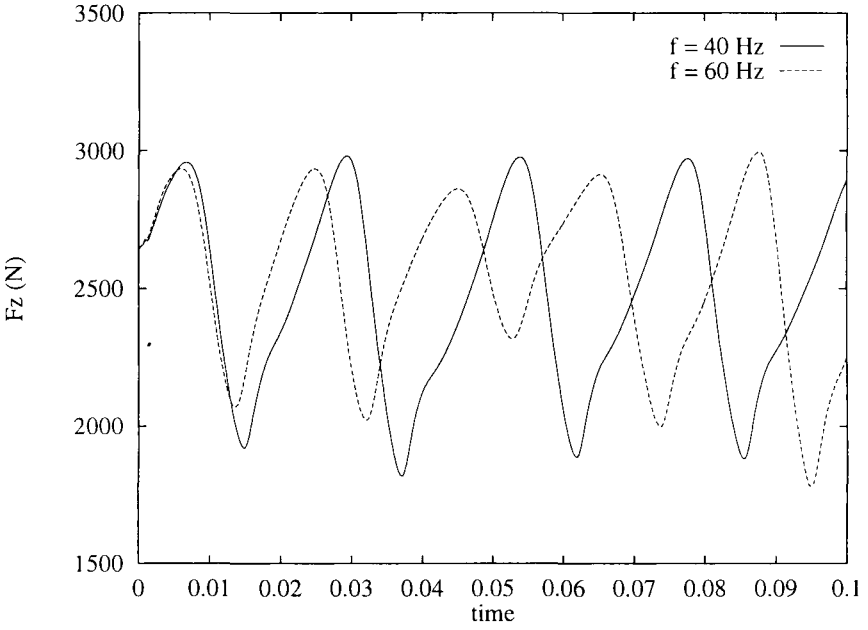

Figure 9. *Unsteady lift*

	x_{cg} (% chord)	m (kg)	I (kg ·m^2)	k_z (N/m)	k_α (N/rad)
Case I	17.0	10.0	9.57×10^{-2}	1.42×10^{6}	1.60×10^{4}
Case II	43.4	10.0	2.18×10^{-1}	1.42×10^{6}	3.64×10^{4}

Table 1. *NACA 64A010 airfoil. Parameters of equivalent mechanical models.*

Both problems are initialized with the steady flow in the fluid domain and with initial translational and rotational velocities of 10^{-4} m/s and 10^{-4} rad/s in the solid domain. A first-order time-marching scheme is used in both domains with a global time-increment $\Delta t = T_\alpha/500$. Figures 14 and 15 present the vertical displacement of the elastic axis and the angle of rotation for Cases I and II. One can note the influence of the center of gravity location on the stability of the fluid-solid system.

3.4. *3D flutter analysis with the DYVAS wing*

Two-dimensional fluid-structure calculations for a NACA064A010 airfoil have demonstrated the validity of the approach described in the second part. Current study

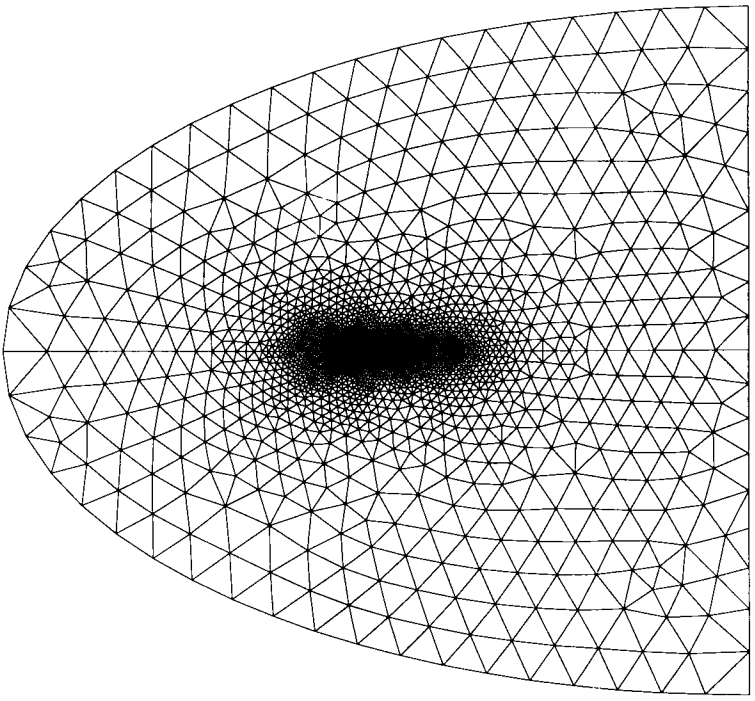

Figure 10. *Fluid mesh for inviscid computation*

now focuses on the DYVAS wing model (see [MOR 91] and references therein).

A structural finite element model has been designed to accurately replicate the dynamics of the experimental wing for the first two modes that are the source of potential flutter. Structural characteristics such as shell thicknesses, section positions and material properties (Young's modulus, density...) have been selected to obtain frequencies and shapes of the first bending and torsion modes at 23.4 Hz and 31.8 Hz, respectively. A system of beams and concentrated masses is used at the root wing to match the experimental modes. Vertical stiffeners between the upper and lower wing surfaces are added along several sections to ensure reasonable rigidity of the wing panels. The solid domain is meshed with about 1900 thin shell elements (see Figure 16).

The fluid domain around the undeformed wing has been discretized with 36,200 nodes and 186,000 tetrahedra.

The computation of the three-dimensional fluid-structure problem is done in two steps:

— 1. First, the coupled static problem is solved to obtain a steady deformed state. The flow is inviscid and is initialized with a uniform field (rather than with the field

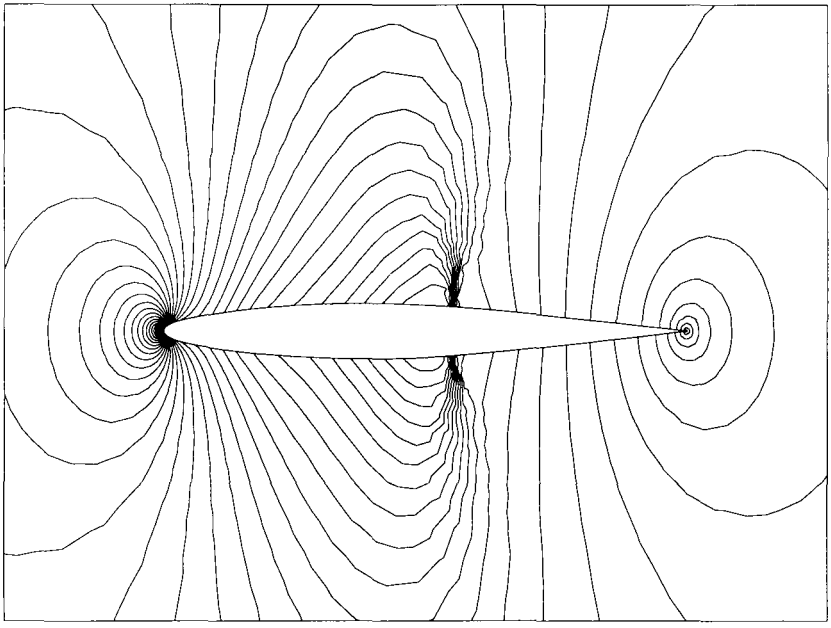

Figure 11. *Inviscid steady pressure contoursFluid mesh for inviscid computation*

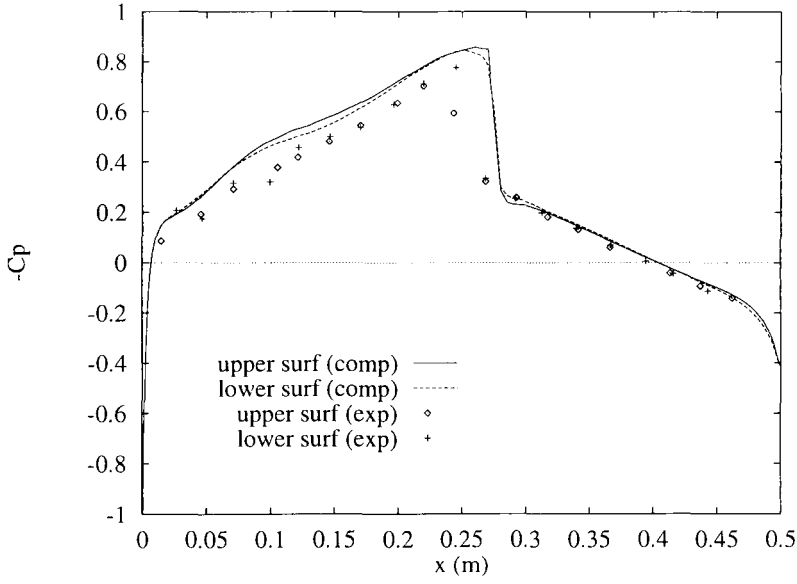

Figure 12. *Inviscid steady pressure distribution on airfoil*

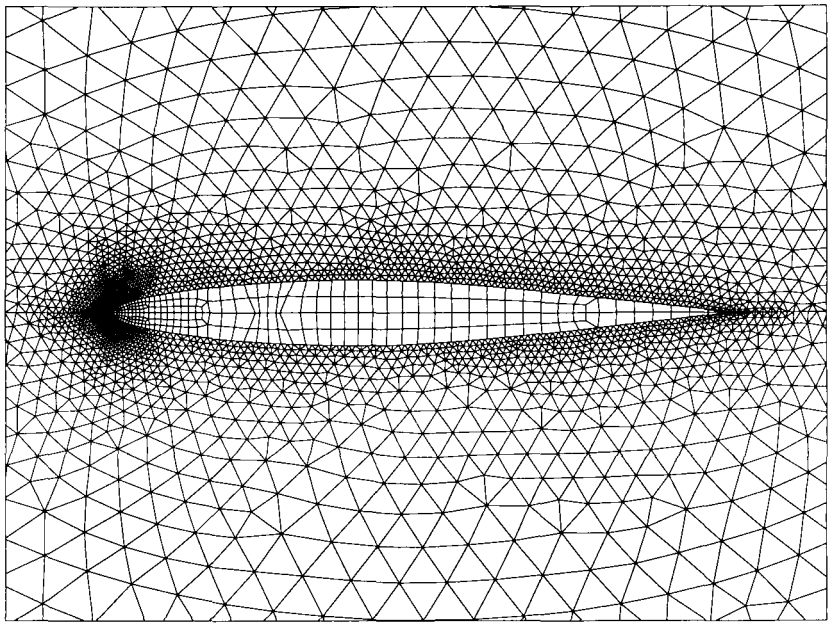

Figure 13. *Fluid and solid meshes in the airfoil vicinity*

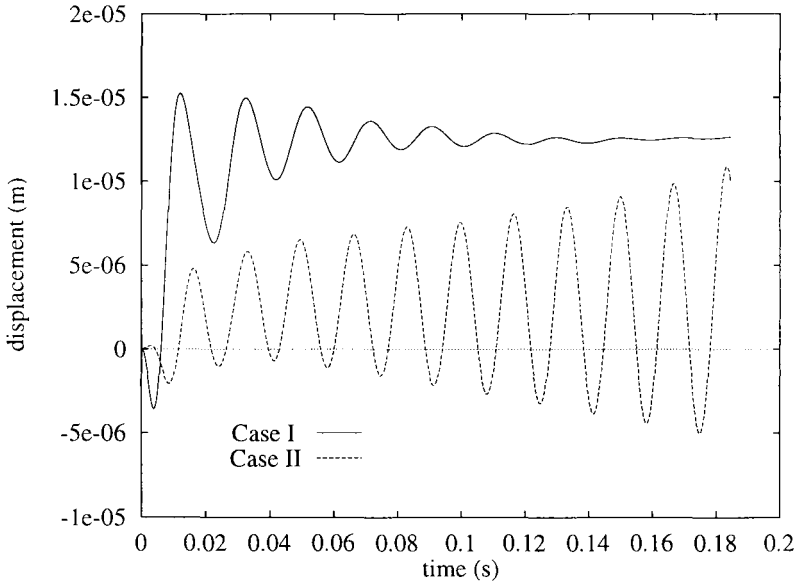

Figure 14. *Vertical displacement of elastic axis*

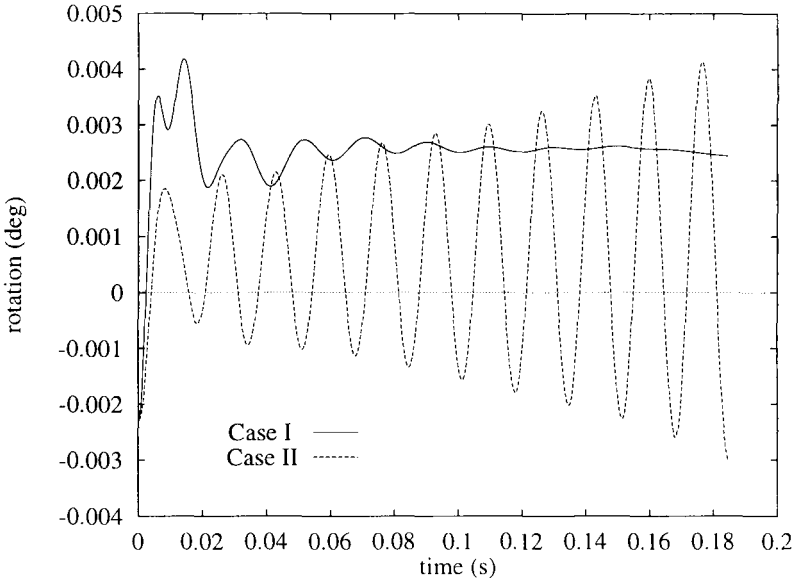

Figure 15. *Rotation of airfoil*

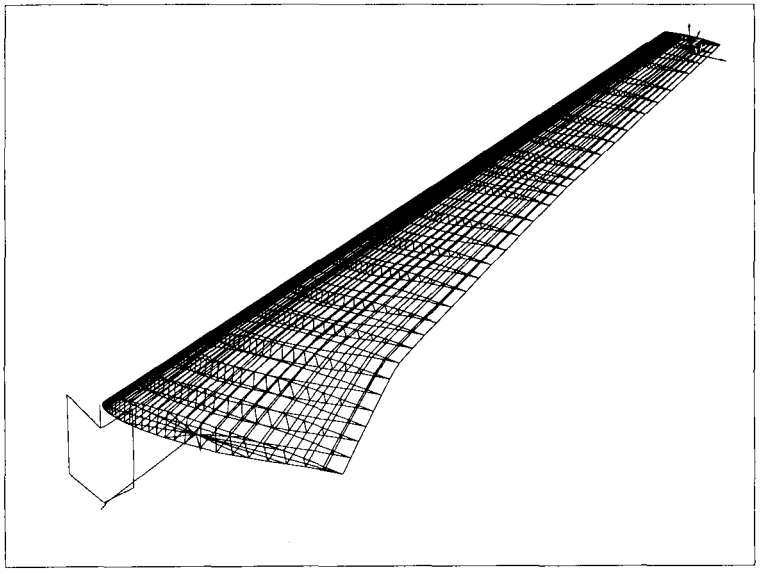

Figure 16. *DYVAS wing solid mesh*

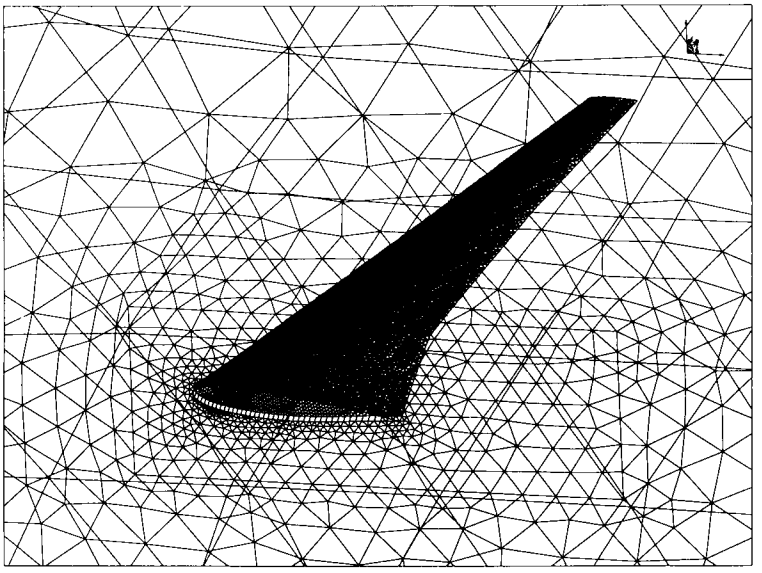

Figure 17. *Fluid mesh around DYVAS wing*

corresponding to the flow around the undeformed wing) to avoid large mesh deformations during the initial time steps. The mesh velocities are not being fed back into the fluid equations [1] to enhance the robustness of the computation. This has no impact on the final solution since we are solving for a steady solution ($\boldsymbol{w} = \mathbf{0}$ at the steady-state limit).

— 2. Once the convergence of the fluid-structure static problem is achieved, flutter analysis is performed: a small vertical force is applied at the wing-tip during the first 4 milliseconds of the computation to excite the first bending mode. The wing is then let free to move. A global time-increment $\Delta t = 4 \times 10^{-4}$ s is used throughout the simulations.

An analysis of the wing displacements is performed using a Fourier transform identification method [PO 91]. One should note that the accuracy of the frequency and damping factor depends mostly on the signal duration. Due to large computation costs, only five to six periods have been computed for each case, which leads to a frequency resolution of 4 Hz only. An improvement of the frequency resolution to 1 Hz would require at least 12 periods.

Two test cases are considered to analyze the behavior of the fluid-structure system. For each free-stream condition, the dynamic pressure is chosen so that the system is either in a stable or an unstable flutter configuration. The fluid flow characteristics and the main results obtained are shown below for both test cases. Wing-tip displacements

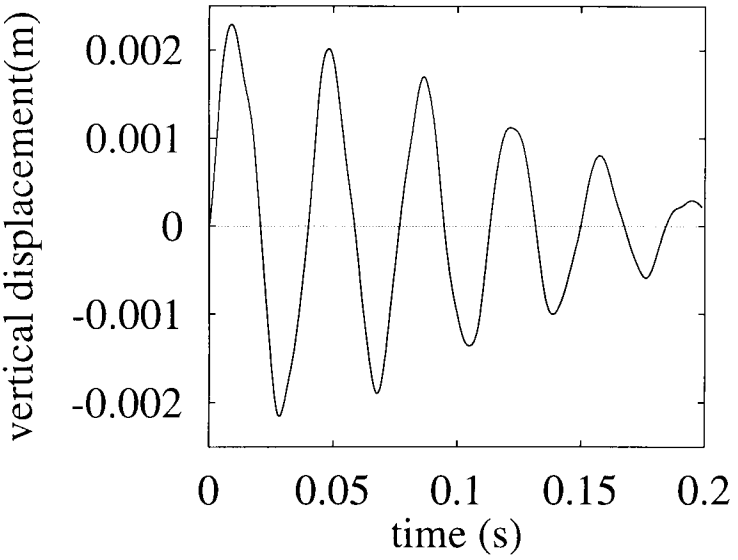

Figure 18. *Wing-tip vertical displacement* ($M_\infty = 0.60$, $P_{i\infty} = 0.9$ *bar*)

are presented in Figures 18 to 21. Frequencies and damping factors are given in Tables 2 to 5.

Case I: $\begin{cases} M_\infty = 0.6 \\ T_\infty = 277.1 \text{ K} \\ \alpha = 1.03° \end{cases}$

Stable case : $P_{i\infty} = 0.9$ bar

Unstable case : $P_{i\infty} = 2.0$ bar

F_{num} (Hz)	α_{num} (damping factor)	F_{exp} (Hz)	α_{exp} (damping factor)
26.4	0.051	26.1	0.056
30.3	−0.010	30.9	0.014

Table 2. $M_\infty = 0.60$, $P_{i\infty} = 0.9$ *bar*
Frequencies and damping factors

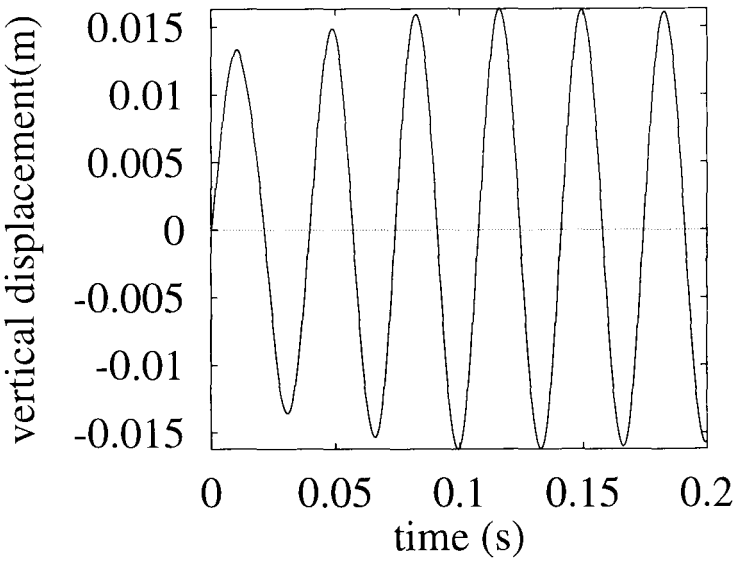

Figure 19. *Wing-tip vertical displacement* ($M_\infty = 0.60$, $P_{i\infty} = 2.0$ *bar*)

F_{num} (Hz)	α_{num} (damping factor)
29.0	0.176
30.0	8.2×10^{-4}

Table 3. $M_\infty = 0.60$, $P_{i\infty} = 2.0$ *bar* *Frequencies and damping factors*

Case II: $\begin{cases} M_\infty = 0.78 \\ T_\infty = 265.7 \text{ K} \\ \alpha = 0.79^\circ \end{cases}$

Stable case : $P_{i\infty} = 0.9$ bar
Unstable case: $P_{i\infty} = 1.5$ bar

F_{num} (Hz)	α_{num} (damping factor)	F_{exp} (Hz)	α_{exp} (damping factor)
29.4	0.0627	28.2	0.057
29.6	3×10^{-4}	30.0	0.019

Table 4. $M_\infty = 0.78$, $P_{i\infty} = 0.9$ *bar* *Frequencies and damping factors*

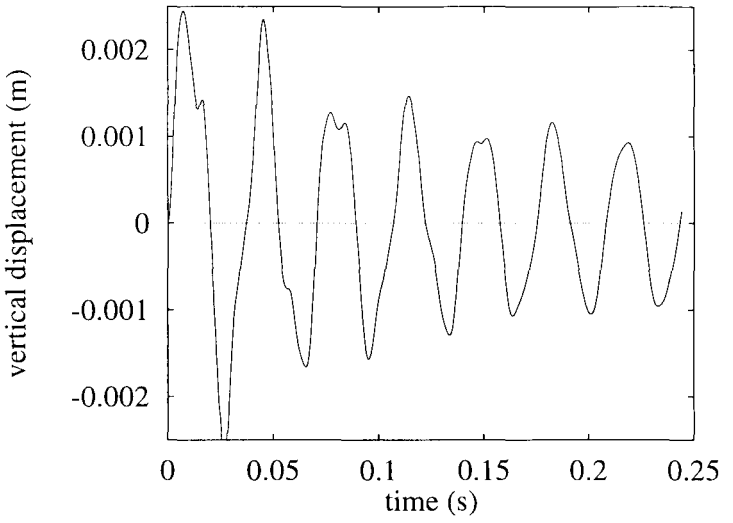

Figure 20. *Wing-tip vertical displacement* ($M_\infty = 0.78$, $P_{i\infty} = 0.9$ *bar*)

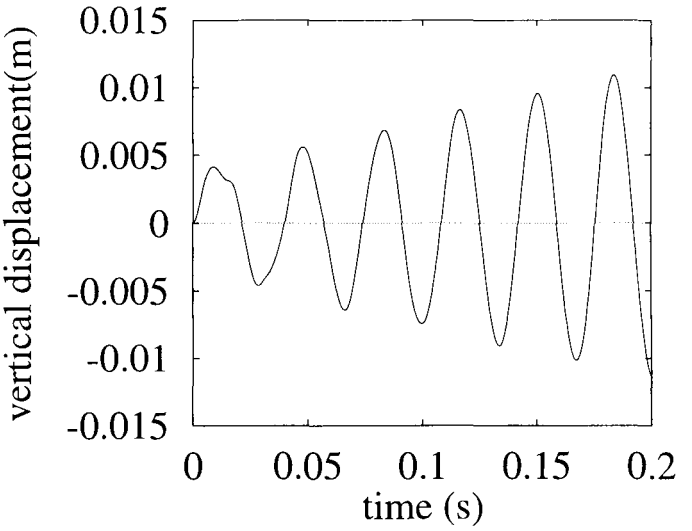

Figure 21. *Wing-tip vertical displacement* ($M_\infty = 0.78$, $P_{i\infty} = 1.5$ *bar*)

F_{num} (Hz)	α_{num} (damping factor)
29.7	−0.0175
30.6	0.1130

Table 5. $M_\infty = 0.78$, $P_{i\infty} = 1.5$ *bar*
Frequencies and damping factors

One can note discrepancies between the computation and the experiments, especially on damping factors. As pointed out above, this is due to poor frequency resolution (about 4 Hz). In both cases, the method gives good results for the most damped mode. However, a signal of greater duration is required to properly separate both frequencies and determine the second mode damping factor precisely.

4. Conclusions

A numerical strategy has been presented to perform aeroelasticity simulations. It has been evaluated for a wide range of applications like buffeting, response to prescribed motion, and fluid-structure flutter problems. The numerical method is based on the Galerkin Least Square Finite Element formulation of both solid mechanical and compressible Euler or Navier-Stokes equations. The same time discretization based on an implicit Newmark's algorithm is then used for both problems. The fluid equations are written in a ALE frame of reference and the fluid mesh modeled as a hyperelastic material is able to deform to make fluid boundaries follow solid boundaries. To take into account the turbulent effects, equations from the Spalart-Allmaras model or from the k-ε model are solved in a staggered fashion with the Navier-Stokes equations. In order to reduce mesh size close to wall, wall functions are added to the turbulence models.

All this strategy has been first applied on buffeting simulation with 2D airfoils. The Spalart-Allmaras turbulence model damps out shock oscillations on upper surface, whereas the k-ε turbulence model gives results close to experimental data, even added with wall functions. Those ones seem then to be a good numerical tool for future 3D simulations with a reasonable number of mesh nodes.

The numerical method described above have been applied to inviscid fluid-structure simulations and to flutter analysis. Dynamic computation was restarted from a steady converged solution. Because of a great number of time-steps per period, it ran on workstation during only few periods, what leads to a poor frequency resolution of few Hz. But results allow us to validate the method for coupling fluid-structure problems. Future works could focus on similar simulations in turbulent flows using wall functions and parallelized algorithms.

5. Aknowledgements

The authors would like to thank the Centric staff for their valuable help throughout this study.

References

[BIS 62] BISPLINGHOFF R.L. et ASHLEY H., *Principles of Aeroelasticity*, John Wiley and Sons, 1962.

[CHI 82] CHIEN K.Y., Predictions of channel and boundary layer flows with a low-Reynolds-number turbulence model. In , *AIAA journal, 20*, 1982 p. 33–38.

[FAR 95] FARHAT C., LESOINNE M. et MAMAN N., Mixed explicit/implicit time integration of coupled aeroelastic problems: three-field formulation, geometric conservation and distributed solution In Eds., *International Journal for Numerical Methods in Fluids, 21*, p. 807–835, Janvier 1995.

[HU 87] HUGHES T.J.R., *The Finite Element Method: Linear Static and Dynamic Finite Element Analysis*, Prentice-Hall 1987.

[HFH 89] HUGHES T.J.R., FRANCA L.P. et HULBERT G.M., A new finite element formulation for computational fluid dynamics: VIII. The Galerkin/least-squares method for advective-diffusive equations, In Eds., *Computer Methods in Applied Mechanics and Engineering, 73*, p. 173–189, 1989.

[HFM 86] HUGHES T.J.R., FRANCA L.P. et MALLET M., A new finite element formulation for computational fluid dynamics: I. Symmetric forms of the compressible Euler and Navier-Stokes equations and the second law of thermodynamics, In Eds., *Computer Methods in Applied Mechanics and Engineering, 54*, p. 223–234, 1986.

[HFM 87] HUGHES T.J.R., FRANCA L.P. et MALLET M., A new finite element formulation for computational fluid dynamics: VI. Convergence analysis of the generalized SUPG formulation for linear time-dependent multidimensional advective-diffusive systems, In Eds., *Computer Methods in Applied Mechanics and Engineering, 63*, p. 97–12, 1987.

[HM 86] HUGHES T.J.R., et MALLET M., A new finite element formulation for computational fluid dynamics: III. The generalized streamline operator for multidimensional advection-diffusion systems, In Eds., *Computer Methods in Applied Mechanics and Engineering, 58*, p. 305–328, 1986.

[MOR 91] MORTCHELEWICZ G.D., Résolution des équations d'Euler tridimensionelles instationnaires en maillage non structuré, In , *La Rcherche Aérospatiale, 6*, 1991 p. 17–25.

[SPA 92] SPALART P.R., et ALLMARAS S.R., A one-equation turbulence model for aerodynamic flows, In , *AIAA paper*, 1992-0439.

[SPE 93] CENTRIC ENGINEERING SYSTEMS, *Spectrum Solver Theory Manual*, 1993.

[LAU 74] LAUNDER B.E., et SPALDING D.B., The numerical computation of turbulent flows, In Eds., *Computer Methods in Applied Mechanics and Engineering, 3*, p. 269–289, 1974.

[WHI 91] WHITE F.M., *Viscous Fluid Flow*, McGraw-Hill 1991.

[MOL 84] MOLINARO R., et SIMON E., Etude instationnaire du décollement sur un profil d'aube dans la soufflerie S3MA, In , *ONERA 03/2894 RNG*, 1984.

[NOT 85] NOTIN C., et SIMON E., Etude de l'écoulement autour d'un profil d'aube de compresseur en régime subsonique, In , *ONERA 34/1621 R 046R*, 1985.

[JOH 91] JOHAN Z., HUGHES T.J.R., et SHAKIB F., A globally convergent matrix-free algorithm for implicit time-marching schemes arising in finite element analysis in fluids, In Eds., *Computer Methods in Applied Mechanics and Engineering, 87*, p. 281–304, 1991.

[BAT 89] BATINA J.T., Unsteady Euler airfoilsolutions using unstructured dynamic meshes, In , *AIAA paper*, 89-0115, 1989.

[DAV 83] DAVIS S.S. , NACA 64A010 (NASA Ames model) oscillatory pitching, In , *Compendium of Unsteady Aerodynamic Measurements*, AGARD Report No. 702,1983.

[PO 91] POIRION F., Analyse des signaux temporels dans l'étude du flottement des avions par la méthode du couplage direct, In , *ONERA Technical Report RT59/3064 RY 101 R*, 1991.